

Mechanical behaviour of connections for cold-formed steel-glass shear wall panels

Bert Van Lancker¹⁾²⁾

Wouter De Corte¹⁾

Jan Belis¹⁾

¹⁾ Magnel-Vandepitte Laboratory, Department of Structural Engineering and Building Materials, Faculty of Engineering and Architecture, Ghent University, Technologiepark-Zwijnaarde 60, B-9052 Zwijnaarde (Ghent), Belgium.

²⁾ Vitroplena – structural glass solutions, Veldstraat 33, B-8740 Pittem, Belgium

Corresponding author

Bert Van Lancker

Phone: +32 473 68 45 70

email: Bert.VanLancker@UGent.be

email: Bert.VanLancker@Vitroplena.com

Abstract

The development of a bonded glass-steel element that is capable to i) transfer out-of-plane loads due to wind loads in transverse direction, ii) in-plane shear loads, due to wind in longitudinal direction and iii) in-plane compression due to self-weight implies that the structural continuous adhesive glass-metal connection becomes an integral part of the entire bonded glass-steel unit. The frame members are restrained by the joint-glass system due to the glass bonded to the steel frame. To assess the capability of continuous adhesive glass-steel connections to transfer the abovementioned loads, research is indispensable. The available knowledge on the capacity of glass panes used as structural bracing element in steel frames is limited. This paper reports about the structural performance of welded steel corners, both not bonded and bonded with glass panes, to assess the in-plane load-bearing capacity of these connections. In a first experimental phase tests on welded steel corners with different configurations are conducted, whilst during the second phase specimens bonded with glass panes on both sides are tested. Numerical models are developed and validated based on the experimental results, which are then used for parametric studies. As such, the rotational stiffness of semi-rigid welded steel corner configurations and the additional stiffness obtained by bonded glass panes can be determined. The results demonstrated that the specimens with adhesively bonded glass panes on both sides using the structural silicones Sikasil® SG-500 and DowSil™ 993, and the hybrid polymer adhesive Soudaseal 2K, significantly increased the initial rotational stiffness of the welded steel corners. Specimens bonded with the hybrid polymer adhesive behave significantly stiffer than specimens bonded with the structural silicones. Parametric studies on validated finite element models reveal that the effect of the glass thickness is important for low values of the adhesive thickness. The width-to-thickness ratio of the adhesive layer largely influences the value of the rotational stiffness of the connection. The generated data by the numerical models can now be implemented in analytical models for the calculation of steel structures with semi-rigid joints.

Keywords: structural silicone, hybrid polymer adhesive, welded connection, width-to-thickness ratio, structural glass

1. Introduction

A closed-cavity façade unit traditionally consists of an outer single glass layer and an inner insulated glass layer which are mechanically connected to an aluminium frame creating the cavity of approximately 20 cm in between. A further optimisation of the structural performance of the glass-framing system is still possible, which can result in a reduced cavity width in favour of net usable floor area, which often has a high impact on the cost of a construction project. This structural optimisation can be realised by using different materials which provide a higher stiffness, by increasing the structural efficiency and/or by increasing the material efficiency.

First, aluminium could be replaced by cold-formed steel as it has a very good strength-to-weight ratio and stiffness-to-weight ratio, resulting in remarkable structural and serviceability performance. Regarding the structural efficiency of the façade unit, cold-formed steel has the advantage that its coefficient of thermal expansion lies significantly closer to the one of glass than the one of aluminium does. Novel continuous adhesive connections, i.e. linear, uniform and uninterrupted adhesive joints with a length that equals multiple times the width, which distribute loads more uniformly than mechanical connections can therefore be developed [1]. These connections have to ensure a durable and reliable transfer of occurring forces, e.g. from wind loads, and have to absorb constraining forces, e.g. from temperature loads. The structural adhesive glass-metal connections can be designed to maximise the involvement of the glass panes in the overall structural behaviour. Material efficiency relates to the use of material properties to their maximum.

Horizontal out-of-plane loads, e.g. frontal wind, need to be transferred by the façade element anyway. However, the potential to transfer horizontal in-plane loads, e.g. lateral wind, and vertical in-plane loads, e.g. self-weight, can be unlocked as well. This would imply that the façade could be self-supporting on the one hand and that it could be partially contributing to the stabilisation of the building on the other. The load-bearing capacities of the glass pane(s) are exploited by making it together with the continuous adhesive glass-metal connections an integral part of the bonded glass-steel façade element. This use of glass as structural element in building construction is expanding rapidly, although there is a lack of standards and design rules. Moreover, the available research on the capacity of glass panes used as structural bracing element in steel frames, i.e. on element level, is limited, making additional research

indispensable. Luible [2] and Enghardt [3] investigated plate buckling of monolithic and laminated glass panes subjected to in-plane compression resulting in the derivation of buckling coefficients for analytical calculations. Wellershoff [4] on the other hand investigated monolithic and laminated glass panels under shear loading deriving buckling factors to determine the critical shear stress. Mocibob [5] developed a shear wall panel with continuous adhesive bond using Dow Corning® 993 at the top and bottom edges. Huveners [6] considered circumferentially adhesively bonded glass panels to a steel frame. A two-sided bonded system using an epoxy adhesive demonstrated the highest potential in terms of in-plane stiffness. Silvestru [7] also investigated circumferentially bonded glass panes to a steel frame. This research made use of a structural silicone and an acrylic adhesive. The acrylate demonstrated a better activation of the load bearing capacities of the glass than the structural silicone.

The development of a (two-sided) bonded glass-steel façade element that is capable to transfer out-of-plane loads (due to wind loads in transverse direction), in-plane shear loads (due to wind in longitudinal direction) and in-plane compression (due to self-weight) as described by Van Lancker [8], implies that the frame members are restrained by the joint-glass system which is integrated in the structural unit. To assess the capability of continuous adhesive glass-steel connections to transfer the abovementioned loads, experimental tests on small-scale test specimens, i.e. component level, allow insight in the structural performance. Numerical modelling allows for further investigation of the effect of geometrical and material parameters on the mechanical behaviour, whereas analytical models enable the development of a (simplified) design approach. Mocibob [5], for example, investigated support concepts for fully transparent pavilions using the aforementioned structural silicone. The connections were tested in tension, transverse shear and longitudinal shear. Single-lap or double-lap shear joint tests are frequently used to assess the mechanical performance of adhesive glass-steel connections, although the dimensions of the specimens are rather arbitrarily chosen due to a lack of standards or technical guidelines. Overend et al. [9], Nhamoinesu et al. [10], Machalicka et al. [11, 12] and Silvestru [13] all performed such tests taking into account a variety of parameters, such as type of adhesive, surface preparation, artificial ageing effects, etc. Katsivalis et al. [14, 15] performed uniaxial tension, uniaxial compression, out-of-plane bending and in-plane bending tests on single-lap and double-lap joint using epoxies and a methacrylate. Differences in the ductility and brittleness of the adhesives lead to different

failure modes ranging from cohesive failure to adhesive failure and glass substrate failure. A modelling methodology was presented to predict the response and failure of the investigated cases.

It is clear that current research on component level is focused on small-scale specimen tests to determine the tensile and shear behaviour of the continuous adhesive bond, to research the interfaces between adhesive and substrates, and to investigate the failure modes of such connections. For circumferentially bonded glass-steel frames, however, the geometry of the adhesive glass-steel joint alters near the corners. Research on the structural performance of these corners of (two-sided) bonded glass-steel frames subjected to an in-plane load on component level gives therefore insight in the local behaviour of the glass-steel joint. Moreover, the combination of data obtained from small-scale single-lap or double-lap shear joint tests and medium-scale corner configuration tests could potentially be sufficient as input for mechanical models to determine the overall structural behaviour of a (two-sided) bonded glass-steel frame subjected to in-plane shear. As such, the number, hence the cost, of full-scale tests for the development of such elements could be significantly reduced. A technical framework and design guidelines could further be elaborated based on the applied novel methodology allowing the introduction of novel bonded glass-steel façade elements into the market. This paper reports about the in-plane structural behaviour of welded steel frame corners, without and with two-sided bonded glass panes using structural silicone and hybrid polymer adhesives. The in-plane force-displacement behaviour is experimentally determined. A first experimental phase consists of tests on welded steel corners with different configurations. The second experimental phase comprises mechanical testing of welded steel corners bonded with glass panes on both sides. Numerical models are developed and validated based on the experimental results, which are then used for parametric studies. As such, the rotational stiffness of semi-rigid welded steel corner configurations and the additional stiffness obtained by bonded glass panes are determined.

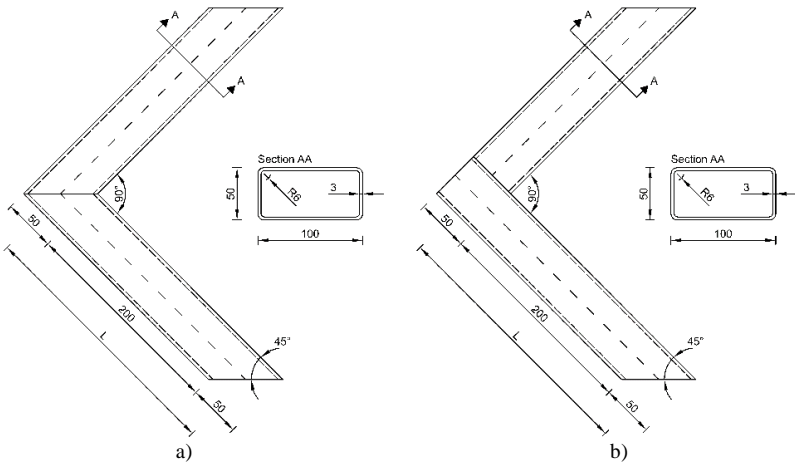
2. Experimental programme (phase 1)

2.1 Material and methods

In a first experimental phase, several tensile and compressive tests are conducted to assess the stiffness of welded connections between thin-walled steel members. Therefore, tubular S235 steel sections, geometrically characterised by a web height h of 100 mm, a flange width w of 50 mm and a thickness

t of 3 mm - also identified as a 100x50x3 section – are welded together considering two different configurations. The first configuration consists of two identically cut sections welded together at an angle of 45° , whilst the second configuration is fabricated using two perpendicularly cut sections welded together at an angle of 90° . A schematic and a photo of the test specimens are given in Fig. 1. At the open ends of the sections, end plates are welded and holes with rounded edge finishing are provided in the centre of these plates to enable the introduction of hinged boundary conditions during testing. Six specimens are manufactured for each weld configuration, i.e. 45° and 90° . Each weld configuration is tested in tension (T) and in compression (C). The identifier of a test series has the general form: weld configuration - type of loading, e.g. 45° -T is the sample containing specimens with sections welded at an angle of 45° tested in tension.

Fig. 2 depicts the test setup for the 45° -configuration in compression and the 90° -configuration in tension with the corresponding free body diagrams. All tests are performed using an Instron 5982 universal testing machine (UTM) with a load cell of 100 kN (accuracy class 0.2%). In compression, steel ball bearings are fitted between the end plates of the specimens and the base plates of the testing machine to introduce a hinged boundary condition. In tension, the specimens are connected to the testing machine using M16 threaded rods and custom-made M16 tapped elements with a rounded edge finish. These custom-made nuts allow for hinged boundary conditions at the end plates of the specimens and at the base plates of the UTM.



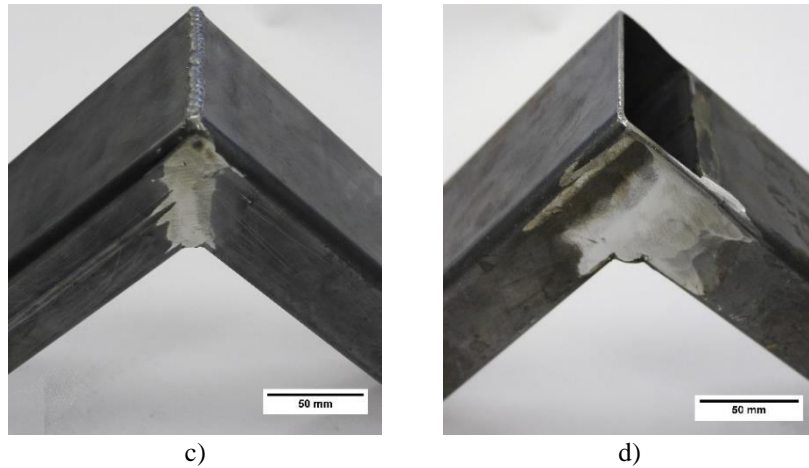


Fig. 1: Schematic and photo of a test specimen for a) c) a 45°-configuration and b) d) a 90°-configuration. Dimensions in mm.

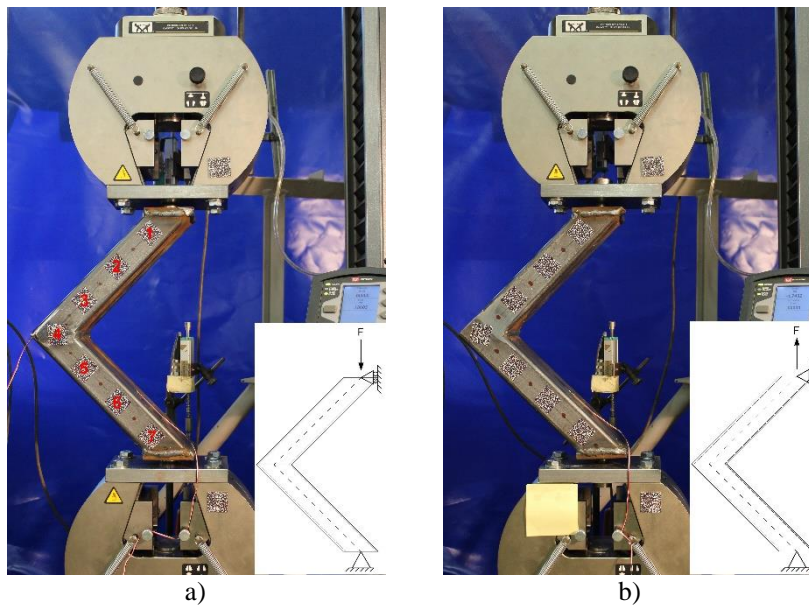


Fig. 2: Test setup during the first experimental phase for a) a 45°-configuration in compression and b) a 90°-configuration in tension (location 1 to 7 for DIC measurements).

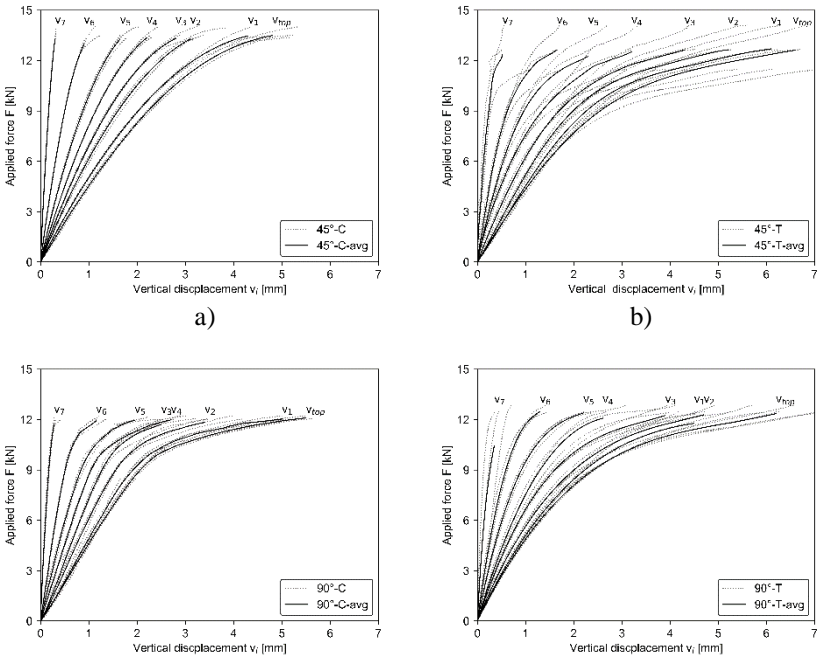
The tests are conducted at ambient temperature and relative humidity in a displacement controlled manner at 5 mm/min until significant nonlinear force-displacement behaviour is observed. Local displacements v_{top} at the top end plate and v_{bottom} at the bottom end plate are measured using linear variable displacement transducers (LVDTs) with a gauge length of 50 mm (accuracy class 0.1%). Digital image correlation, as described in detail in [8, 16], is used to measure the in-plane deformations of the steel sections at discrete points along their length. The displacements of the pneumatic wedge action grips are measured to enable calibration and to minimise measurement uncertainty. A speckle pattern was generated using a Speckle Generator and applied to the steel sections at seven different locations, i.e. location 1 to 7 in Fig. 2 a). Pictures are taken at regular time intervals using a Canon EOS 500D SLR camera with an EF-S-18-55 mm f/3.5-5.6 IS lens. During testing, 350 ohm uniaxial strain gauges with

one measuring grid (accuracy 1%) applied on the steel sections measured the occurring strains under the applied load as a verification of the validity of the adopted analytical model (see Section 2.2) to calculate the rotational stiffness of the welded steel corner configuration.

2.2 Results and discussion

2.2.1 Experimental results

Fig. 3 depicts the experimental relationship between the applied force F [kN] and the vertical displacements v_{top} [mm] and v_1 [mm] to v_7 [mm] of the steel sections at the seven locations for all configurations tested, i.e. 45°-C, 45°-T, 90°-C and 90°-T. The force-displacement curves of each individual test as well as the average ($N = 3$) curve is included. For compression, no vertical displacement at the bottom end plate is measured during the entire test, i.e. $v_{bottom} = 0$. The vertical displacement v_{UTM} of the crosshead of the UTM equals therefore the vertical displacement v_{top} measured by the LVDT. For tension, the vertical displacements of the bottom end plate differ from zero due to the presence of the M16 threaded rods, i.e. $v_{bottom} \neq 0$. All measured displacements v_{top} and v_1 to v_7 are therefore corrected to have the bottom end plate as reference point. Remark that the dispersion in results is much larger for the tensile tests than for the compression tests. This can possibly be attributed to the higher susceptibility of the tensile test setup to measurement errors, i.e. the derived displacements are based on the measurements of two LVDTs compared to only one for the compressive test setup.



c) d)

Fig. 3: Individual and average ($N = 3$) relationship between applied force F [kN] and vertical displacement v_{top} [mm] and v_1 [mm] to v_7 [mm] of the steel sections at the seven locations for a) 45°-C, b) 45°-T, c) 90°-C and d) 90°-T.

2.2.2 Analytical representation

The stiffness of the steel corner configuration is derived from the relationship between the applied force F and the corrected vertical displacement v_{top} of the top end plate. Therefore, the experimental test setup is represented by an analytical model to determine the initial rotational stiffness C_0 (see below).

The analytical model is validated by the measured deformations and strains during testing.

2.2.2.1 Model description

As depicted in Fig. 4, the two steel members with length L , as designated in Fig. 1, and bending stiffness EI are connected in the common node B by a rotational spring with spring stiffness C . A vertical roller bearing is present in node A and a hinged connection is present in node C, representing the bounding conditions during testing. A compressive (see Fig. 4 a)) or tensile (see Fig. 4 b)) force F is acting vertically in node A. The slope-deflection method is used to determine the deformations in the system in terms of bar rotations Ψ and joint rotations φ from which joint or node displacements can be calculated. Here, normal force deformations are neglected, as well as second order effects, such as the P- δ -effect (local deformations relative to the element chord between end nodes) and P- Δ -effect (displacement of the member ends). Shear force deformations are neglected as well as they will be less than 5% as the ratio of the height of the members to the length of the members is equal to $50/250 = 1/5$ [17].

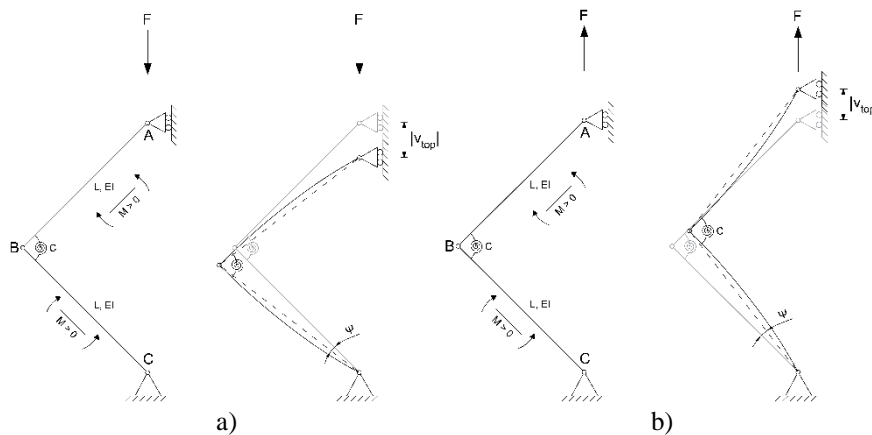


Fig. 4: Wire model of welded steel corner configurations loaded a) in compression or b) in tension and the corresponding deformations v_{top} , Ψ and φ .

The observer is assumed to be positioned left and below steel member BC, which determines the sign convention as depicted in Fig. 4. Initially, the unknown variables are the bar rotations Ψ_{AB} and Ψ_{BC} , and the joint rotations φ_A , φ_{BA} , φ_{BC} , φ_C . Due to symmetry, Ψ_{AB} and Ψ_{BC} will be identical except for the sign, as expressed in Eq. (1).

$$-\Psi_{AB} = \Psi_{BC} = \Psi \quad \text{Eq. (1)}$$

All fixed end moments are zero as no forces are acting between the joints. The slope deflection equations are expressed by Eq. (2) to Eq. (5).

$$\overline{M}_{AB} = \frac{2EI}{L}(2\varphi_A + \varphi_{BA} + 3\Psi) \quad \text{Eq. (2)}$$

$$\overline{M}_{BA} = \frac{2EI}{L}(2\varphi_{BA} + \varphi_A + 3\Psi) \quad \text{Eq. (3)}$$

$$\overline{M}_{BC} = \frac{2EI}{L}(2\varphi_{BC} + \varphi_C - 3\Psi) \quad \text{Eq. (5)}$$

$$\overline{M}_{CB} = \frac{2EI}{L}(2\varphi_C + \varphi_{BC} - 3\Psi) \quad \text{Eq. (6)}$$

Node A, B and C should comply with equilibrium conditions. In node A and C the end moments are, due to the boundary conditions, equal to zero as expressed in Eq. (7) and Eq. (8). In node B, the acting member end moments are counteracted by the presence of the rotational spring. The counteracting moments are function of the rotational spring stiffness C and the joint rotations φ_{BA} and φ_{BC} , resulting in the equilibrium equations as expressed in Eq. (9) and Eq. (10).

$$\overline{M}_{AB} = 0 \quad \text{Eq. (7)}$$

$$\overline{M}_{CB} = 0 \quad \text{Eq. (8)}$$

$$\overline{M}_{BA} = -C\varphi_{BA} \quad \text{Eq. (9)}$$

$$\overline{M}_{BC} = -C\varphi_{BC} \quad \text{Eq. (10)}$$

A final equilibrium equation can be determined based on Fig. 5 a), which is valid for compression. Expressing the bending moment equilibrium about point P results in Eq. (11). Similarly, Eq. (12) can be derived in case of tension, i.e. for an inverted sense of direction of the force vector in Fig. 5.35 a). The shear force V_{BC} can be expressed as function of the moments \overline{M}_{BC} and \overline{M}_{CB} through Eq. (13). This equation represents the moment equilibrium of the forces on the free-body diagram of member BC about node C, as depicted in Fig. 5 b).

$$\overline{M}_{BC} - V_{BC} + \sqrt{2}LF = 0 \quad \text{Eq. (11)}$$

$$\overline{M}_{BC} - V_{BC} - \sqrt{2}LF = 0 \quad \text{Eq. (12)}$$

$$V_{BC} = -\frac{\overline{M}_{BC} + \overline{M}_{CB}}{L} \quad \text{Eq. (13)}$$

Eq. (7) to Eq. (10) and Eq. (11) can be solved for the unknown variables resulting in Eq. (14) to Eq. (16) for compression. These equations also apply for the tensile loading case, except for the sign of the expressions.

$$\varphi_A = -\varphi_C = -\frac{\sqrt{2} FL(CL+2EI)}{6 CEI} \quad \text{Eq. (14)}$$

$$\varphi_{BA} = -\varphi_{BC} = -\frac{\sqrt{2} FL}{2 C} \quad \text{Eq. (15)}$$

$$-\Psi_{AB} = \Psi_{BC} = \frac{\sqrt{2} FL(CL+3EI)}{6 CEI} \quad \text{Eq. (16)}$$

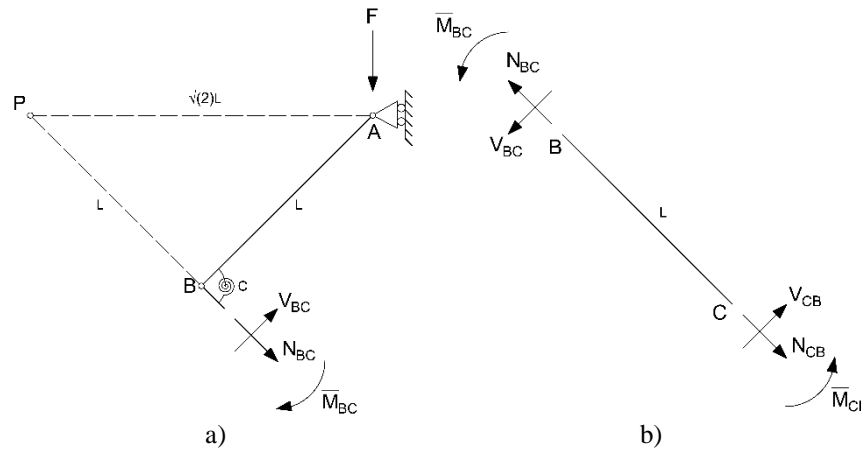


Fig. 5: a) The free-body diagram of the corner configuration under compression for which the moment equilibrium about point P results in Eq. (5.41) and b) the free-body diagram of member BC for which the moment equilibrium about node C results in Eq. (5.43).

As the bar rotations and joint rotations are known, joint displacements can easily be determined. The vertical displacement of node A can be calculated using Eq. (17), hence the rotational stiffness C can be calculated from this displacement using Eq. (18). When the rotational stiffness C equals zero, the system becomes a mechanism, i.e. $|v_{top}|$ equals infinity. When the rotational stiffness tends to infinity, the connection between the steel members becomes moment-resisting or rigid. This implies that the angle between the tangent lines to the deformation lines in the connection remains 90° when the system is loaded. For that, the denominator in Eq. (18) has to equal zero which implies that $|v_{top}|$ equals FL^3/EI . This is indeed the displacement at the top in the statically determined system assuming rigid connections, which can easily be verified using the principles of virtual work [17].

$$|v_{top}| = \sqrt{2} |\Psi_{AB}| L = \frac{FL^2(CL+3EI)}{3CEI} \quad \text{Eq. (17)}$$

$$C = -\frac{3EIFL^2}{FL^3 - 3|v_{top}|EI} \quad \text{Eq. (18)}$$

By substituting Eq. (14) to Eq. (16) in Eq. (3) to Eq. (6), the bending moments in the steel members can be calculated using Eq. (19) to Eq. (22).

$$M_{AB} = \overline{M}_{AB} \quad \text{Eq. (19)}$$

$$M_{BA} = -\overline{M}_{BA} \quad \text{Eq. (20)}$$

$$M_{BC} = -\overline{M}_{BC} \quad \text{Eq. (21)}$$

$$M_{CB} = \overline{M}_{CB} \quad \text{Eq. (22)}$$

At the top and bottom end section, the bending moments are zero due to the hinged boundary condition. Near the welded connection of both steel members, the absolute value of the bending moments equals $\sqrt{2}FL/2$. Fig. 6 illustrates the bending moment diagram in the corner configuration when loaded in compression and in tension. The total displacement of a random physical point along the length of the members can be calculated based on the known bar rotation Ψ and the bending moment distribution in the steel member.

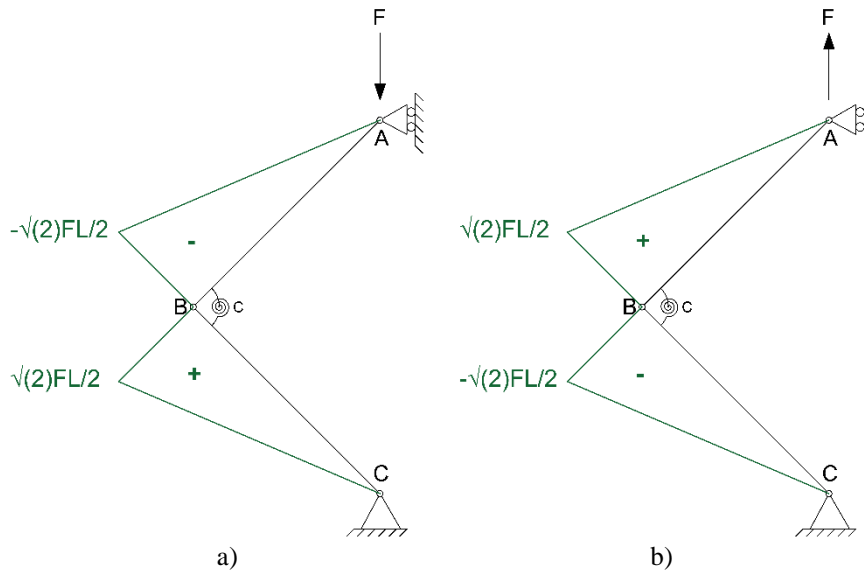


Fig. 6: Bending moment diagram in the welded steel corner configurations loaded in a) compression and b) tension. As presented in Fig. 6, the bending moments near the welded connection of both steel members equal in absolute value to $\sqrt{2}FL/2$, whilst the bending moments near the top and bottom end plate equal zero. This implies that the absolute value of the bending moment at a random location x along the length of the steel member starting from an end plate is expressed as Eq. (23).

$$|M(x)| = \frac{\sqrt{2}Fx}{2} \quad \text{Eq. (23)}$$

According to the Euler-Bernoulli beam theory [18], the stress σ in a cross-section x subjected to simple bending $M(x)$ at a point of interest that lies at distance z from the neutral axis, i.e. beam axis that

encounters zero stress, can be calculated according to Eq. (24) with I the second area of moment of the cross-section. Corresponding to the adopted sign convention, positive stresses correspond to tensile stresses, whilst negative stresses are compressive stresses.

$$\sigma(x, z) = \frac{M(x)z}{I} \quad \text{Eq. (24)}$$

To convert the theoretical stresses σ to theoretical strains ε , Hooke's law for linear elastic materials from solid mechanics, as expressed in Eq. (25) with E the material's Young's modulus, is applied, which results in Eq. (26).

$$\sigma = E\varepsilon \quad \text{Eq. (25)}$$

$$\varepsilon(x, z) = \frac{M(x)z}{EI} \quad \text{Eq. (26)}$$

2.2.2.2 Model validation

As a validation of the adopted method, the vertical displacements v_1 to v_7 are analytically calculated using the slope-deflection method with the experimental relation between the applied force F and the measured displacement v_{top} at the top end as input. Hence, the experimentally obtained instantaneous rotational stiffness C [kNm/rad], i.e. Eq. (18) applied for each experimental datum point (F, v_{top}) , is implemented in the analytical equations. These analytical relations can be plotted against the experimental relations between the applied force F [kN] and the measured displacements v_1 to v_7 by means of digital image correlation. Fig. 7 depicts the comparison between the average ($N = 3$) analytical and experimental relation between the applied force F [kN] and the vertical displacement v_{top} [mm] of the top end plate and the vertical displacements v_1 [mm] to v_7 [mm] for all configurations. Note that the nonlinear behaviour of the analytical solution is a consequence of the nonlinear experimental force-displacement curve that serves as input for the analytical model, which only assumes linear elastic material behaviour (see below). A good agreement is observed, and thus the adopted assumptions and analytical model are valid to determine the rotational stiffness C of corner configurations based on experiments.

Remark that the experimental force-displacement relationship is not linear due to geometrically nonlinear and material nonlinear behaviour, hence the rotational stiffness C will not be a constant in se. However, an initial rotational stiffness C_0 can be derived when taking into account the linear part of the force-displacement curve. Fig. 8 depicts the linear approximation of the average force-displacement

behaviour at the top end plate, and the comparison between the experimentally obtained average force-displacement curve at node 4, i.e. near the welded connection between the members, and the analytically determined relationship based on the initial rotational stiffness C_0 . The analytical calculations implementing the initial rotational stiffness C_0 demonstrate excellent agreement with the linear part of the experimentally obtained force-displacement curves at a random point along the length of one of the steel members.

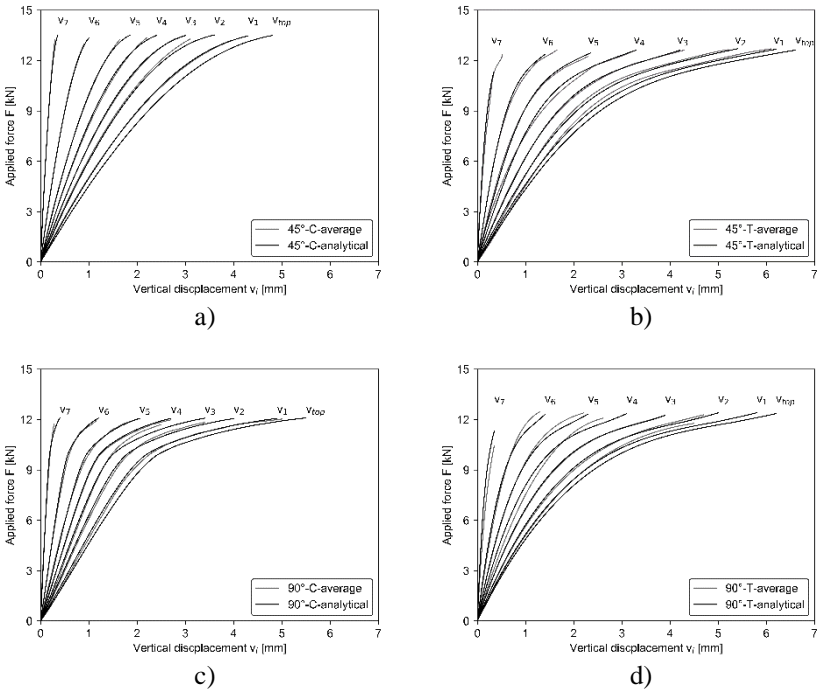
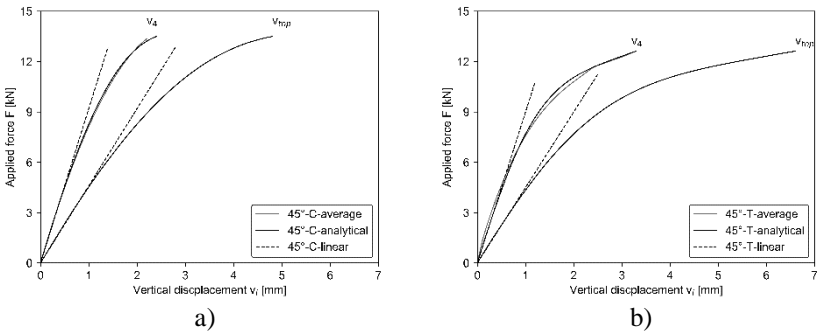


Fig. 7: Average ($N = 3$) experimental and analytical relationship between applied force F [kN] and vertical displacement v_{top} [mm] and v_1 [mm] to v_7 [mm] of the steel sections at the seven locations for a) 45°-C, b) 45°-T, c) 90°-C and d) 90°-T.



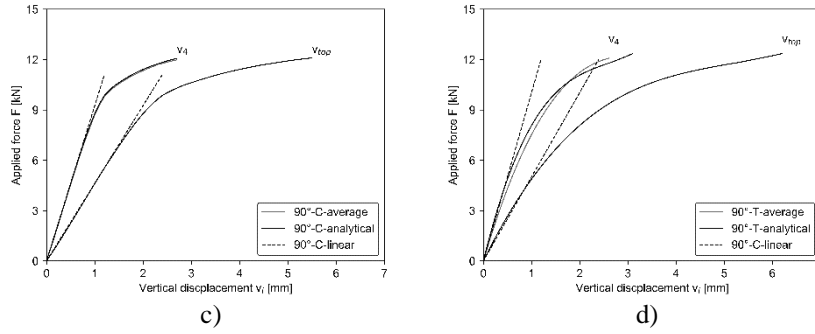


Fig. 8: Average ($N = 3$) experimental and analytical relationship between applied force F [kN] and vertical displacement v_{top} [mm] and v_4 [mm] of the steel sections and average linear approximation for a) 45°-C, b) 45°-T, c) 90°-C and d) 90°-T.

Applying Eq. (26) to the experimentally tested corner configurations using 100x50x3 steel sections implies that the Young's modulus E equals 210000 MPa, the second moment of inertia I equals 360571 mm⁴ and the point of interest z equals -25 mm or +25 mm, i.e. bottom or top surface of the cross-section. The first specimen of each sample was provided with one strain gauge on the top member and one strain gauge on the bottom member. The second and third specimen of each sample are provided with one strain gauge each, on the top member and on the bottom member respectively. Fig. 9 depicts the applied load F [kN] as function of the experimentally measured strains ε [10^{-6}] at the measurement locations as well as the analytically determined strains ε [10^{-6}] using Eq. (26) for all tested configurations. Remark that results from tensile tests demonstrate greater dispersion than from compression tests (see above).

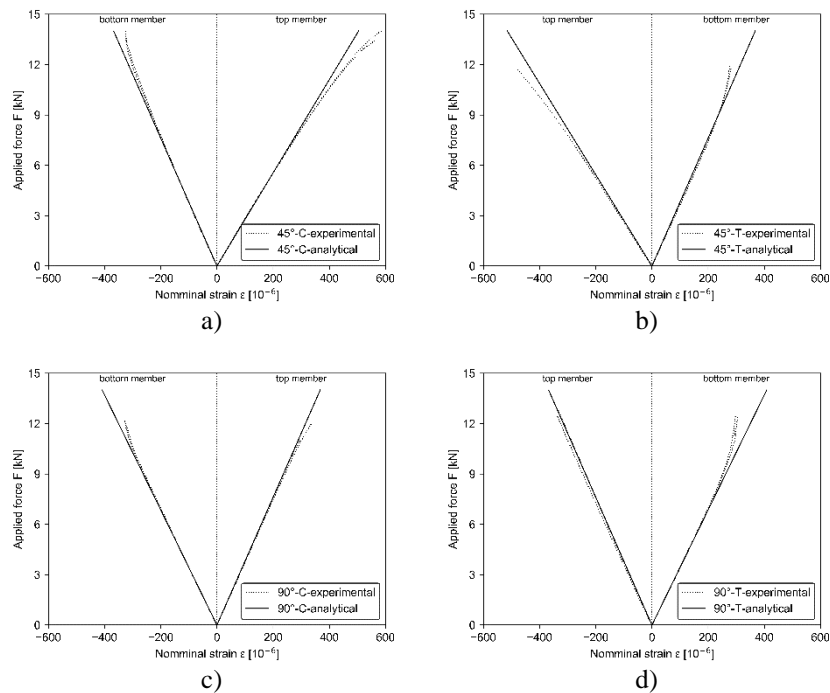


Fig. 9: Experimental and analytical strains ε [10^{-6}] related to the applied force F [kN] in the top and bottom member for a) 45°-C, b) 45°-T, c) 90°-C and d) 90°-T.

2.2.3 Initial rotational stiffness $C_{0,avg}$

Table 1 summarises the average ($N = 3$) initial rotational stiffness $C_{0,avg}$ [kNm/rad] for both the 45°-configuration and 90°-configuration tested in both compression and tension. The difference in average rotational stiffness value for 45°-C and 45°-T is not statistically significant ($\alpha = 5\%$). This can be attributed to the symmetry of this welded corner configuration. Between 90°-C and 90°-T, a significant difference in average stiffness value exist, most probably due to the asymmetry of the corner configuration. The 90°-C-configuration has a comparable initial rotational stiffness as the 45°-configurations.

Table 1: Average ($N = 3$) initial rotational stiffness $C_{0,avg}$ [kNm/rad] for 45°-configuration and 90°-configuration tested in compression (C) and tension (T).

Test series	45°-C	45°-T	90°-C	90°-T
$C_{0,avg}$ [kNm/rad]	420.92±27.49	419.28±18.82	424.66±24.60	478.66±9.97

3. Experimental programme (phase 2)

3.1 Material and methods

A second experimental phase is elaborated to assess the stiffness of welded connections between thin-walled steel members stiffened with two-sided bonded glass panes. Therefore, 100x50x3 S235 steel sections are welded together. Based on the experimental results from Section 2.2, the configurations with the highest measured initial rotational stiffness in compression and tension are selected, i.e. a 45°-configuration tested in compression and a 90°-configuration tested in tension. Again, end plates are welded at the open ends of the specimens and rounded edge finished holes are provided in the centre to enable the introduction of hinged boundary conditions during testing. A total of nine specimens for the 45°-configuration and nine specimens for the 90°-configuration are manufactured. For each configuration, three specimens are bonded using the structural silicone Sikasil® SG-500 (SI500), another three specimens are bonded using the structural silicone DowSil™ 993 (DS993) and the remaining three specimens are bonded using the hybrid polymer adhesive Soudaseal 2K (SO2K). The two-component structural adhesives, for which the basic properties are presented in Table 2, are selected based on previous research [2, 8]. Note that the mechanical properties of the adhesives are derived from uniaxial tensile tests on H-specimens in accordance to ETAG 002 as described by Van Lancker [8].

Table 2: Mechanical properties of the selected adhesives derived from uniaxial tensile tests on H-specimens [8].

Property	Sikasil [®] SG-500 (SI500)	DowSil [®] 993 (DS993)	Soudaseal 2K (SO2K)
Density ρ [kg/m ³]	1400	1300	1400
Tangential modulus E_0 [MPa]	3.17	4.24	4.73
Poisson coefficient ν [-]	0.462	0.490	0.495
Tensile strength f_t [MPa]	2.19	1.67	1.44
Strain at break [%]	134	113	100

A sketch of the fabricated specimens and a detail photo of the corner configurations are presented in Fig. 10. Before bonding, the steel sections are thoroughly cleaned using isopropyl alcohol and acetone. Next, the first bonding surface is cleaned and primed using the cleaner and primer corresponding to the specific adhesive used for bonding. 275 mm by 275 mm monolithic annealed float glass panes with a nominal thickness t_{gl} of 10 mm are degreased and cleaned using isopropyl alcohol. The bonding surface, i.e. the air side of the glass panes, is determined using a UV-lamp. A cavity of 36 mm between the glass panes and the welded steel sections is created using Thermalbond[®] V2100, a polyurethane foam spacer, with a width of 8 mm. The foam spacer has a nominal thickness of 6.4 mm for the structural silicones and 3.2 mm for the hybrid polymer adhesive. The glass panes are positioned and the created cavities are filled with adhesive material using automated dispensing guns. The specimens are held in horizontal position for 24 hours at ambient temperature and relative humidity. Afterwards, the specimens are turned over and the second glass pane is bonded to the welded steel sections according to the aforementioned procedure. After another 24 hours at ambient temperature and relative humidity, the finished specimens are transported to the test facility, where they are stored for another seven days in a climatic chamber with a temperature of $20 \pm 1^\circ$ C and a relative humidity of $60 \pm 3\%$. Fig. 11 depicts the test setup for bonded specimens tested in compression and in tension, which is identical to the setup used during the first experimental phase (see Section 2.1). The tests are conducted in a displacement-controlled manner at 5 mm/min ($\dot{\gamma}_{SI500} = \dot{\gamma}_{DC993} = 0.37/\text{min}$, $\dot{\gamma}_{SO2K} = 0.75/\text{min}$) at ambient temperature and relative humidity. Vertical displacements of the top and bottom end plates, i.e. v_{top} and v_{bottom} , are measured using LVDTs (accuracy class 0.1%) with a gauge length of 50 mm. The general form of the identifier of a test series is: adhesive - weld configuration - type of loading, e.g. SI500-45[°]-C is the sample containing specimens with sections welded at an angle of 45[°] bonded with Sikasil[®] SG-500 and tested in compression. Note that only 45[°]-C and 90[°]-T series exist in contrast to the former experimental phase (see Section 2).

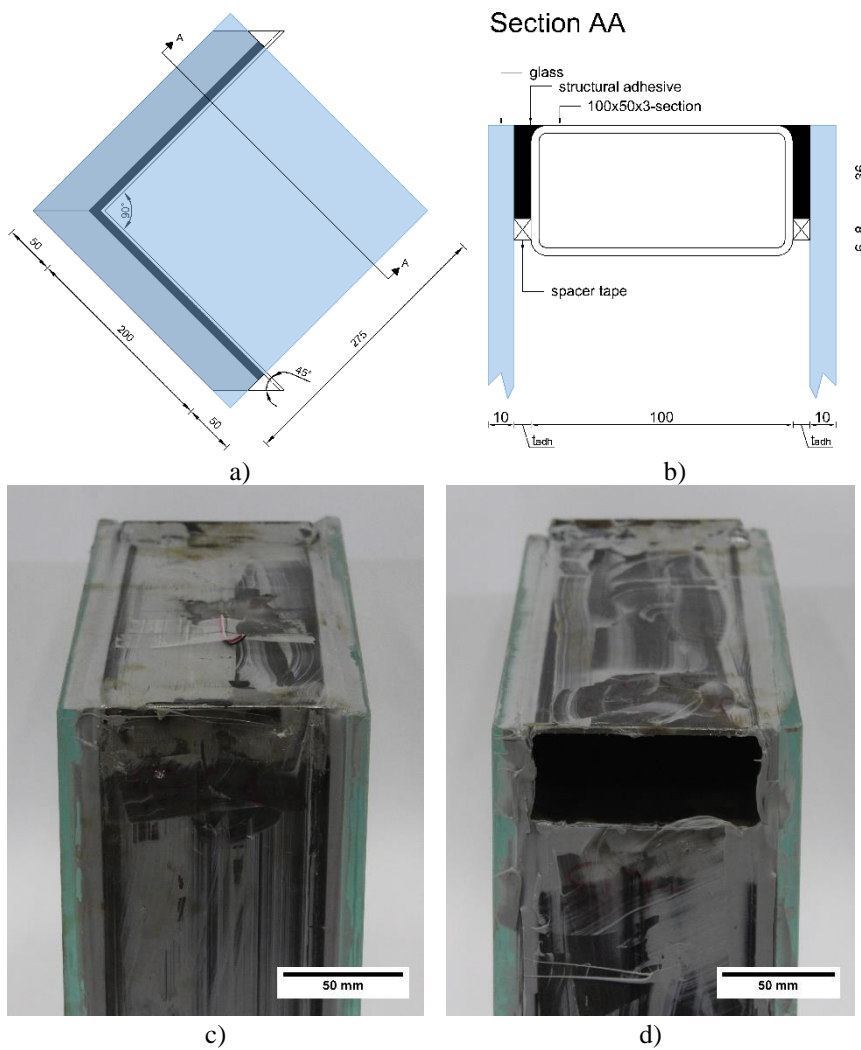
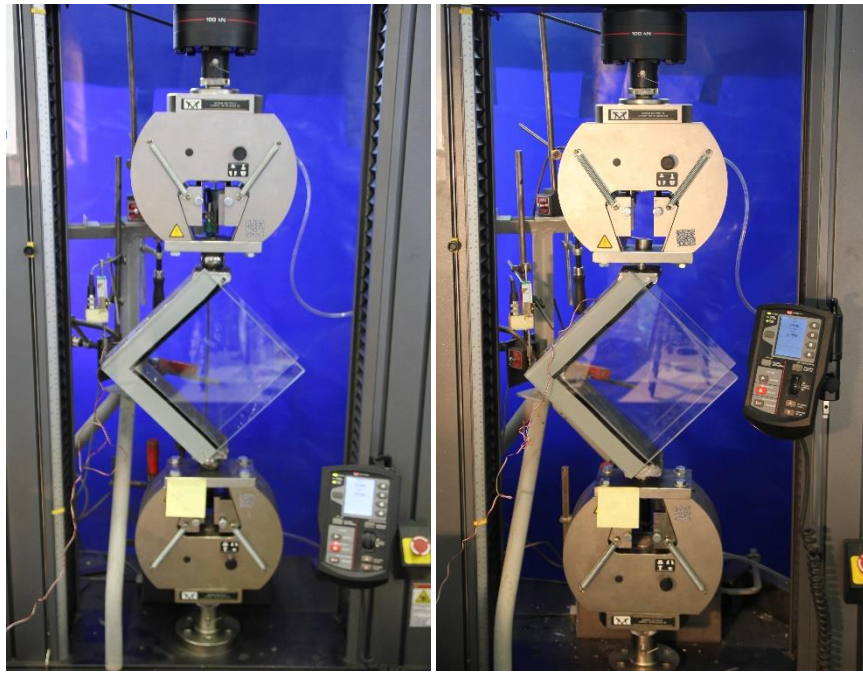


Fig. 10: Schematic representation of a) b) a specimen from the second experimental phase (t_{adh} is the nominal thickness of the adhesive layer, i.e. 6.4 mm for SI500 and DS993, and 3.2 mm for SO2K) and detailed photos of c) a 45°-configuration and d) a 90°-configuration. Dimensions in mm.



a)

b)

Fig. 11: Test setup during the second experimental phase for a) a 45°-configuration in compression and b) a 90°-configuration in tension.

3.2 Results and discussion

During testing, progressive cohesive failure for all specimens is observed. In the adhesive layer, a crack forms when the maximum of the load is reached. With increasing displacements, the crack propagates through the adhesive layer, together with the formation of new ones until the metal section partially or completely segregates from the glass pane.

In case of the 45°-C-configurations, cohesive shear failure starts at the top and/or bottom end plate, where shear is at its maximum. For two out of three specimens for each adhesive, glass breakage in one or two panes occurs afterwards. The other specimens fails purely cohesively. For the bonded specimens with a 90°-T-configuration, cohesive failure in the adhesive layer is observed for DS993 and SO2K. Local buckling of the bottom steel member is observed as well. In case of SI500-90°-T, glass breakage occurs after initial cohesive failure near the top and bottom end plate and local buckling of the bottom steel section. Fig. 12 depicts the failure modes of the bonded specimens tested in compression and tension for all adhesives considered.

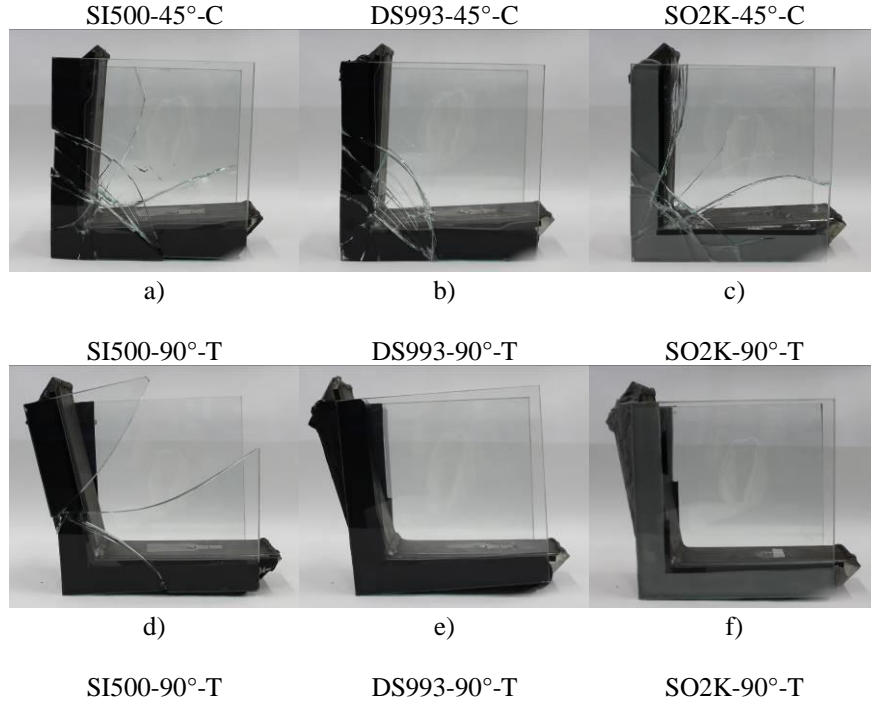


Fig. 12: Failure mode of a) SI500-45°-C, b) DS993-45°-C, c) SO2K-45°-C, d) SI500-90°-T, e) DS993-90°-T and f) SO2K-90°-T.

Table 3 summarises the average ($N = 3$) values of the maximum applied load F_{max} [kN] for the non-bonded specimens at which yielding already occurred and the failure loads for the different test series with bonded specimens. The bonded specimens demonstrate a significant ($\alpha = 5\%$) increase in maximum applied load compared to non-bonded specimens. Only for SI500 a significant difference is observed between the 45°-C-configuration and the 90°-T-configuration. For the 45°-C-configuration, the type of adhesive significantly affects the ultimate load as well, which is not the case for the 90°-T-configuration. However, note that the standard deviation for the 90°-T-configuration has a significantly greater value than for the 45°-C-configuration (see Table 2).

Table 3: Average ($N = 3$) maximum applied load F_{max} [kN] for 45°-configuration and 90°-configuration tested in compression (C) and tension (T).

Test series		45°-C	SI500-45°-C	DS993-45°-C	SO2K-45°-C
F_{max}	[kN]	13.64±0.34	16.56±0.74	20.26±0.51	22.08±0.90
Increase	[%]	-	21.4	48.5	61.9
Test series		90°-T	SI500-90°-T	DS993-90°-T	SO2K-90°-T
F_{max}	[kN]	12.59±0.24	21.62±2.04	23.24±2.00	21.86±1.44
Increase	[%]	-	58.5	70.4	60.3

Fig. 13 depicts the relationship between the applied force F [kN] and the vertical displacement v_{top} [mm] for all bonded specimens tested in 45°-C-configuration and 90°-T-configuration for a limited displacement range. Similarly as done in Section 2.2, the measured displacements v_{top} are corrected to

have the bottom end plate as reference point. Fig. 13 a) and b) demonstrate the stiffer behaviour of the bonded specimens with the hybrid polymer adhesive compared to the ones with structural silicones. It could be noted that the nominal thickness of the adhesive layer for the specimens with SO2K is 3.2 mm compared to 6.4 mm for the specimens with SI500 and DS993. Further, the mechanical behaviour of the bonded specimens with SI500 and DS993 is similar for both the 45°-C-configuration and the 90°-T-configuration.

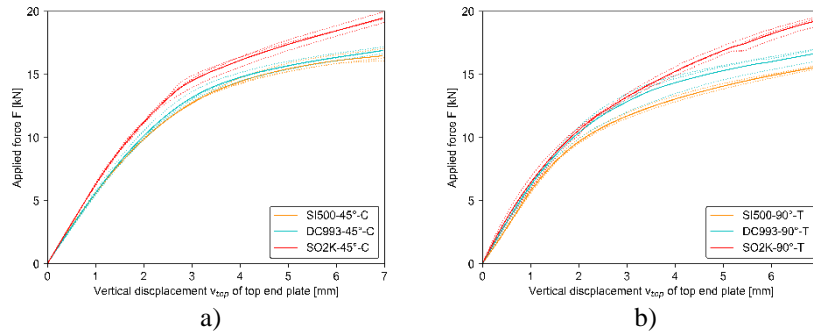


Fig. 13: Relationship between the applied load F [kN] and the vertical displacement v_{top} [mm] of the top end plate for bonded specimens using SI500, DS993 and SO2K tested in a) 45°-C-configuration and b) 90°-T-configuration. To assess the increase in stiffness of the welded corner configurations due to two-sided bonding with glass panes, the initial rotational stiffness $C_{0,avg}$ is determined using Eq. (18) in which the initial part of the force-displacement curve is linearised. Remark that the bending stiffness EI implemented in the equations equals the bending stiffness of the steel sections and not the one of the hybrid bonded steel-glass cross-section. This is done because only the additional stiffness of the bonded glass panes to the initial stiffness of the welded steel corner configuration is investigated. Table 3 comprises the average ($N = 3$) initial rotational stiffness $C_{0,avg}$ [kNm/rad] for the 45°-configuration tested in compression and the 90°-configuration tested in tension for both non-bonded and bonded specimens. What Fig. 13 graphically indicates, is presented by the values of the initial rotational stiffness $C_{0,avg}$ [kNm/rad] in Table 4. No statistically significant ($\alpha = 5\%$) difference can be observed for bonded specimens with either SI500 or DS993 nor for the 45°-C-configuration or 90°-T-configuration. Bonded specimens with SO2K have a significantly higher initial rotational stiffness $C_{0,avg}$ compared to the specimens with SI500 or DS993. This is caused by the stiffer behaviour of the adhesive itself and the reduced thickness of the adhesive layer, i.e. 3.2 mm for SO2K compared to 6.4 mm for SI500 and DS993. For SO2K, no significant differences are detected by comparing different configurations and load directions.

Table 4: Average ($N = 3$) initial rotational stiffness $C_{0,avg}$ [kNm/rad] for 45°-configuration and 90°-configuration tested in compression (C) and tension (T).

Test series	45°-C	SI500-45°-C	DS993-45°-C	SO2K-45°-C
$C_{0,avg}$ [kNm/rad]	420.92±27.49	596.50±22.24	589.52±28.84	700.89±10.05
Increase [%]	-	41.7	40.1	66.5
Test series	90°-T	SI500-90°-T	DS993-90°-T	SO2K-90°-T
$C_{0,avg}$ [kNm/rad]	478.66±9.97	587.72±17.7	603.99±9.60	709.45±16.28
Increase [%]	-	39.6	43.5	68.5

4. Numerical investigation

4.1 model and validation

A three-dimensional finite element model is built in Abaqus® to numerically investigate the stiffness of welded steel corner configurations, whether or not stiffened with bonded glass panes using structural silicone and hybrid polymer adhesives. Fig. 14 depicts the numerical model for a bonded specimen with the steel sections welded in a 45°-configuration. The length of the steel members is chosen equal to five times the width of the section to exclude a significant effect of shear force deformation (see above).

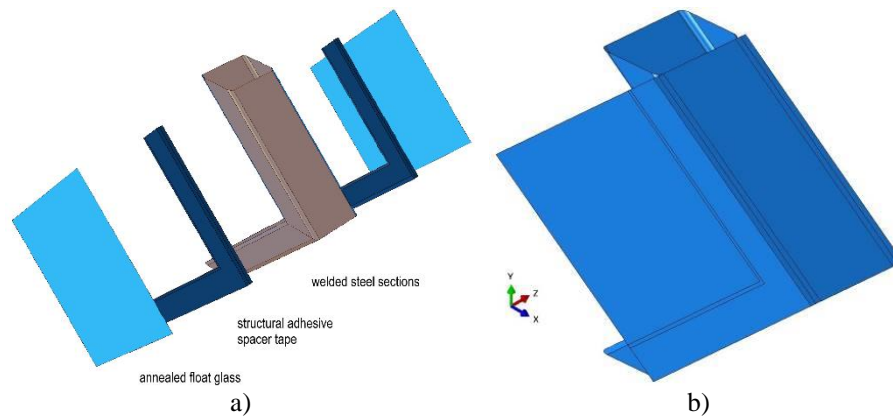


Fig. 14: a) Exploded view and b) assembly for the numerical model to investigate the rotational stiffness of welded steel corner configurations stiffened with two-sided bonded glass panes.

Glass is modelled as a linear elastic material with a Young's modulus of 70 GPa and a Poisson's ratio of 0.23 [19]. Steel is modelled as an elastic material with a Young's modulus equal to 210 GPa and a Poisson coefficient of 0.3 [20]. In case of bonded specimens, polyurethane foam tape acting as spacer is modelled linear elastically with a modulus of elasticity equal to 0.9 MPa in accordance with the recommendations of the manufacturer. To implement the hyperelastic material behaviour of the adhesives, a preliminary investigation on the suitability and validity of the material models as presented by Van Lancker et al. [21] for this specific bonded glass applications is performed. Therefore, the ten best material models from that work are selected for each adhesive and implemented in Abaqus® using either user-defined subroutines with dependent state variables or direct implementation methods. For

SI500, the hyperelastic material model of Ogden calibrated for the combination of tension-compression-shear gives the best results for the 45°-C-configuration, whilst the material model of Yeoh calibrated based on tensile tests performs the best for the 90°-T-configuration. In case of DS993, the models of Mooney-Rivlin and Ogden, both calibrated for shear, re selected for the 45°-C-configuration and 90°-T-configuration respectively. For bonded specimens with SO2K, the hyperelastic material model of Van der Waals calibrated for tension and shear performs the best for the 45°-C-configuration. For the 90°-T-configuration with SO2K, the model of Arruda-Boyce for the combination tension-compression-shear is selected to represent the material behaviour of the adhesive in this bonded glass application.

The steel sections are connected to each other using a tie-constraint. The adhesive layer in the finite element model is connected to the glass panes and the steel sections by means of tie-constraints with the adhesive layer as slave in the master-slave surface definition of the constraint. Note that cohesive interfaces would be more appropriate when failure loads are derived from the numerical model. Here focus lies on the force-displacement relation and the stiffness of the connection derived from that relationship. The mesh of the adhesive layer is hex-dominated using C3D20RH elements. The spacer tape was modelled using C3D20R elements. The glass panes and the steel sections are modelled using S4R shell elements. A convergence study is performed to investigate the optimal mesh size and element size ratio. To represent the end plates, reference points are introduced in the centre of gravity of the end cross-sections of the steel members. Using a tie-constraint between reference point and the edges of the end cross-section, the restricted movement of the end cross-section due to the end plate is modelled. The boundary condition at the bottom end plate is introduced in the reference point and allows only for rotational movement, not translational movement, i.e. a hinged connection. At the top, a concentrated force acts on the reference point representing the introduced load during the tests.

General, static step-by-step numerical analyses are performed using the implicit Abaqus[®] solver. To validate the numerical models before using them for parametric studies, a comparison is made between numerical and experimental load-displacement relationship, and between the nominal strains in Abaqus[®] and the strains measured by the strain gauges on the steel members during the experiments. Table 5 compares the experimentally and numerically determined initial rotational stiffnesses C_0 [kNm/rad] of the connections for both non-bonded and bonded specimens. As significant agreement

between the results from the finite element models and the experimental results exist, the model is considered validated to determine the initial rotational stiffness of these connections. Note that also the measured strains compared to the numerically determined strains show good agreement [8].

Table 5: Comparison between experimentally and numerically determined initial rotational stiffness C_0 .

Test series	45°-T	45°-C	SI500-45°-C	DC993-45°-C	SO2K-45°-C
$C_{0,avg}$ [kNm/rad]	419.28±18.82	420.92±27.49	596.50±22.24	589.52±28.84	700.89±10.05
$C_{0,FEA}$ [kNm/rad]	424.81	422.25	596.20	589.32	698.03
Δ [%]	1.3	0.3	0.1	0.0	0.4
Test series	90°-C	90°-T	SI500-90°-T	DC993-90°-T	SO2K-90°-T
$C_{0,avg}$ [kNm/rad]	424.66±24.60	478.66±9.97	587.72±17.70	603.99±9.60	709.45±16.28
$C_{0,FEA}$ [kNm/rad]	425.81	476.10	586.34	604.27	714.43
Δ [%]	0.3	0.5	0.2	0.0	0.7

4.2 parametric study

The validated numerical models for non-bonded and bonded welded steel corner configurations enable a thorough investigation of the effect of geometrical and material parameters on the rotational stiffness of the connections. For the non-bonded specimens, variations in the section's web height h [mm], flange width w [mm] and wall thickness t [mm] are investigated as represented in Table 6. As no statistically significant difference between the behaviour of configurations 45°-C, 45°-T and the 90°-C for the non-bonded specimens is detected during the experiments, the parametric study is limited to the 45°-C-configuration and the 90°-T-configuration.

Table 6: Investigated parameters in finite element analyses of non-bonded corner configurations (reference case in bold).

Configuration	web height h [mm]	Flange width w [mm]	Section thickness t [mm]
45°-C	50, 60, 80, 100 , 120, 140,	20, 30, 40, 50 ,	2, 3 , 4, 5
90°-T	150, 160, 180, 200	60, 80, 100	

Fig. 15 depicts the initial rotational stiffness C_0 [kNm/rad] of the 45°-C-configuration as function of the area moment of inertia I [10^6 mm^4] of the sections for all investigated section thicknesses t . Identically, Fig. 16 represents these relationships for the 90°-T-configuration. The corner configuration exhibits stiffer mechanical behaviour with increasing section thickness. An increase in section thickness results in a larger weld area and in a larger second area of moment. The vertical displacements at the top decrease with increasing section thickness. Overall, the result based on Eq. (18) is an increased initial rotational stiffness. When considering a fixed web height of the section, the initial rotational stiffness

increases with increasing flange widths due to significant increases in the area moment of inertia and significant decreases of the vertical displacement of the top end plate. On the other hand, the stiffness decreases with an increasing web height of the section when considering a fixed flange width. The vertical displacements at the top do decrease with increasing web height. However, combined with a significant increase in second area of moment, the overall result based on Eq. (18) is a lower initial rotational stiffness of the corner configuration.

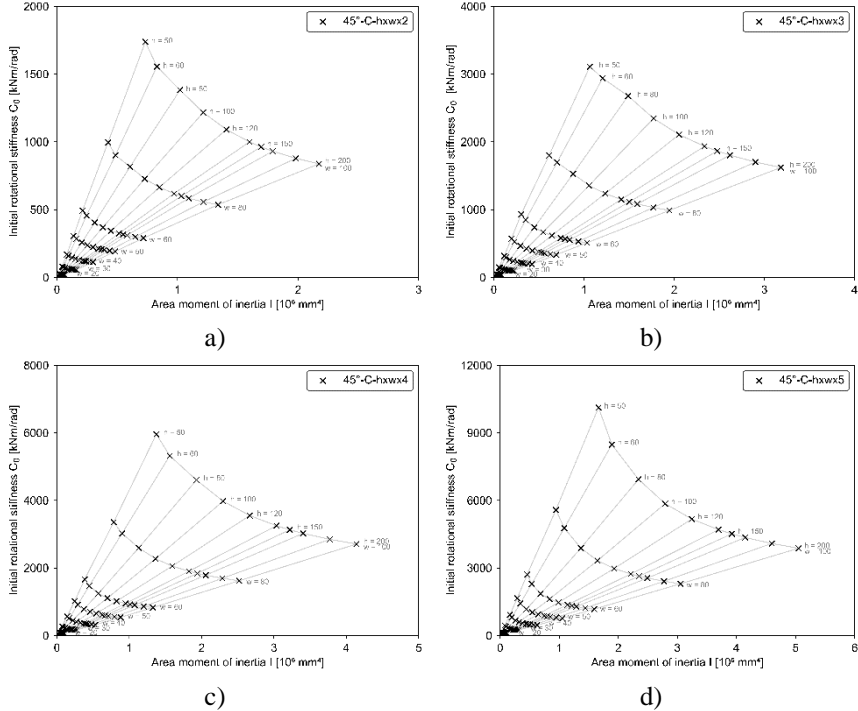
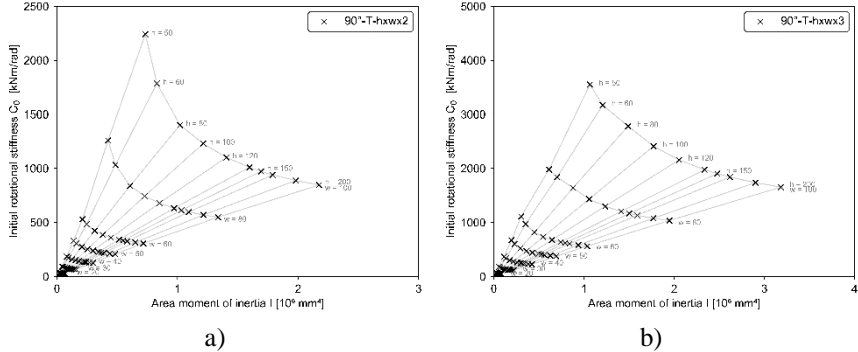


Fig. 15: Initial rotational stiffness C_0 [kNm/rad] as function of the area moment of inertia I [10^6 mm^4] of the steel sections for the 45°-C-configuration for a section thickness t equal to a) 2 mm, b) 3 mm, c) 4 mm and d) 5 mm.



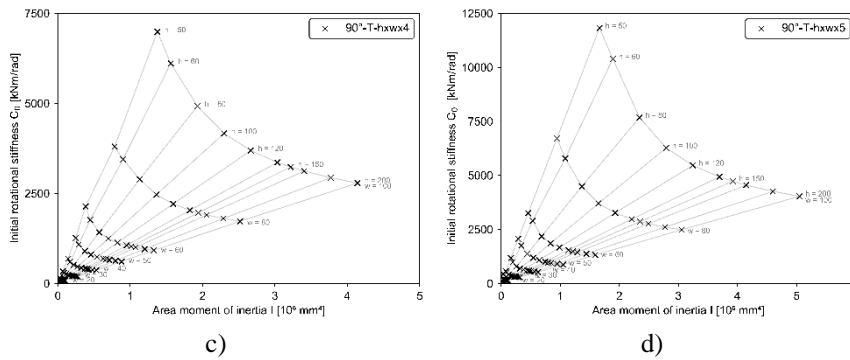


Fig. 16: Initial rotational stiffness C_0 [kNm/rad] as function of the area moment of inertia I [10^6 mm^4] of the steel sections for the 90° -T configuration for a section thickness t equal to a) 2 mm, b) 3 mm, c) 4 mm and d) 5 mm.

Fig. 15 and Fig. 16 can be utilised to determine the initial rotational stiffness C_0 [kNm/rad] of a 45° or 90° welded corner configuration with random steel sections geometrically characterised by a web height h [mm], a flange width w [mm] and a thickness t [mm]. First, the set of figures for the desired configuration, i.e. 45° or 90° , has to be selected, then the figure for the required section thickness t [mm]. In the retained figure, the curve for a certain flange width w [mm] or a certain web height h [mm] can be nominated, after which the initial rotational stiffness C_0 [kNm/rad] can be determined as function of web height h [mm] or flange width w [mm], respectively. For intermediate values, linear interpolation can be applied to obtain sufficiently accurate results. Once the initial rotational stiffness C_0 [kNm/rad] is determined, calculations of structural steel elements, e.g. frames, using these semi-rigid connections can be performed.

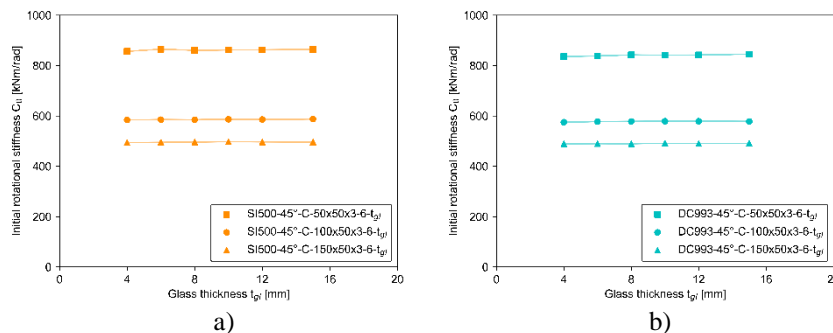
For the investigation of the effect of geometrical parameters on the rotational stiffness of bonded specimens, a selection of geometries for the steel sections mentioned in Table 7 is withheld. The effect of the adhesive thickness and the glass thickness is also investigated. Table 7 mentions the investigated adhesive thicknesses t_{adh} [mm] and glass thicknesses t_{gl} [mm]. Varying adhesive widths or joint bites are associated with varying section flange widths. As the experiments demonstrate that there is no significant difference between 45° -configurations tested in compression and 90° -configurations tested in tension, only the 45° -C-configuration is considered for the parametric study of bonded corner configurations. However, it should be noted that the finite element model for a 90° -T-configuration is validated as well and is as such applicable for the determination of an initial rotational stiffness C_0 [kNm/rad] of such bonded corner configurations. The identifier of a simulation of a bonded specimen has the general form: adhesive - weld configuration - type of loading - steel section - adhesive thickness

t_{adh} [mm] - glass thickness t_{gl} [mm], e.g. SI500-45°-C-100x50x3-6-10 is the simulation with 100x50x3 tubular sections welded at an angle of 45° bonded with two 10 mm thick glass panes using Sikasil® SG-500 with an adhesive thickness of 6 mm tested in compression. Note that the weld configuration – load direction for this parametric study is fixed and is always 45°-C.

Table 7: Investigated adhesive thicknesses t_{adh} [mm] and glass thicknesses t_{gl} [mm] in finite element analyses of bonded corner configurations (reference case in bold).

Adhesive	Adhesive thickness t_{adh} [mm]	Glass thickness t_{gl} [mm]
SI500	2, 4, 5, 6 , 7, 8, 10, 12, 15, 20	4, 6, 8, 10 , 12, 15
DS993		
SO2K	1, 2, 3 , 4, 5, 6, 8, 10, 12, 15	

Fig. 17 represents the initial rotational stiffness C_0 [kNm/rad] as a function of the glass thickness t_{gl} [mm] for configurations with 50x50x3, 100x50x3 and 150x50x3 steel sections for all investigated adhesives individually, as well as a comparison between the adhesives for a configuration with 100x50x3 steel sections. Fig. 17 demonstrates the negligible effect of the glass thickness for SI500 and DS993. In case of SO2K, an increase in initial rotational stiffness with an increase in glass thickness is observed. Remark that the adhesive layer for the structural silicones has a thickness of 6 mm, whilst for the hybrid polymer adhesive, this thickness is only 3 mm. Hence, it appears that the influence of the glass thickness on the initial rotational stiffness is of importance for low values of the adhesive thickness (see below). The corner configuration, furthermore, behaves more flexible for an increased web height, although there is an increase in second area of moment and weld area (see below). Comparing the structural silicone and hybrid polymer adhesives mutually, it is demonstrated that the structural silicones behave similar, whilst the hybrid polymer adhesive exhibits stiffer behaviour due to the recommended use of practice.



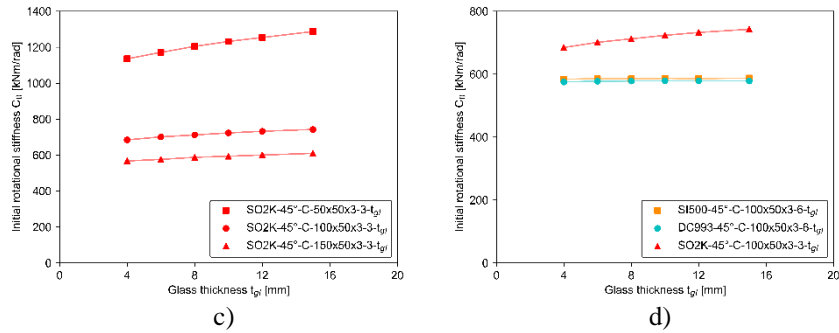
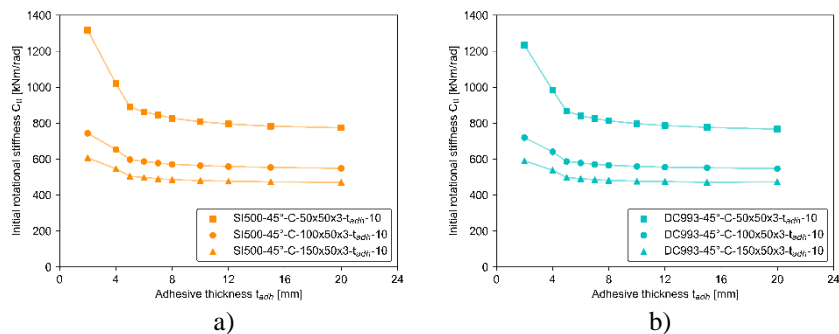


Fig. 17: Initial rotational stiffness C_0 [kNm/rad] for configurations with 50x50x3, 100x50x3 and 150x50x3 steel sections as function of the glass thickness t_{gl} [mm] for a) SI500, b) DS993, c) SO2K and d) a comparison between adhesives for configurations with 100x50x3 steel sections.

Fig. 18 depicts the relationship between the initial rotational stiffness C_0 [kNm/rad] and the thickness t_{adh} [mm] of the adhesive layer for configurations with 50x50x3, 100x50x3 and 150x50x3 steel sections for all investigated adhesives. Also a comparison between adhesives for the configurations with 100x50x3 steel sections is represented. The influence of the adhesive thickness is most important for values below 5 mm. Below this value, also the glass thickness has a non-negligible effect as aforementioned. The initial rotational stiffness remains unaffected for larger values of the adhesive thickness, whereby the glass thickness also loses its importance. Again, the corner configuration demonstrates a stiffer behaviour when the web height of the steel sections decreases. Fig. 18 d) demonstrates that the difference in initial rotational stiffness between adhesives for a fixed adhesive thickness is insignificant. However, in practice, hybrid polymer adhesives will be applied as a thinner adhesive layer than the structural silicones, resulting in stiffer behaviour.



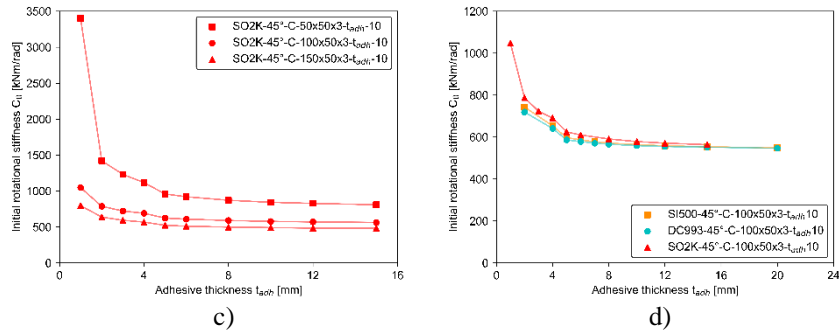


Fig. 18: Initial rotational stiffness C_0 [kNm/rad] for configurations with 50x50x3, 100x50x3 and 150x50x3 steel sections as function of the adhesive thickness t_{adh} [mm] for a) SI500, b) DS993, c) SO2K and d) a comparison between adhesives for configurations with 100x50x3 steel sections.

The influence of the web height h [mm] on the initial rotational stiffness C_0 [kNm/rad] for all investigated adhesives is illustrated in Fig. 19 a). Fig. 19 b) depicts the relationship between initial rotational stiffness C_0 [kNm/rad] and the flange width w [mm] of the steel section, which is related to the adhesive bite B [mm]. An increase in web height results in a decrease of the initial rotational stiffness, which was also detected by interpreting Fig. 17 and Fig. 18. An increase in flange width, which results in an increase in adhesive bite, rapidly increases the value of the initial rotational stiffness. A further increase in adhesive bite will result in a value of C_0 equal to infinity, as illustrated in Fig. 19 b), which implies that the corner configuration behaves as a completely stiff connection. Similarly, a further decrease in web height will theoretically result in a corner configuration which will behave as a completely stiff connection as well, i.e. C_0 tends towards infinity in Fig. 19 a). A web height equal to zero means theoretically that only the glass panes would be present, which indeed would result in an infinite value of the initial rotational stiffness.

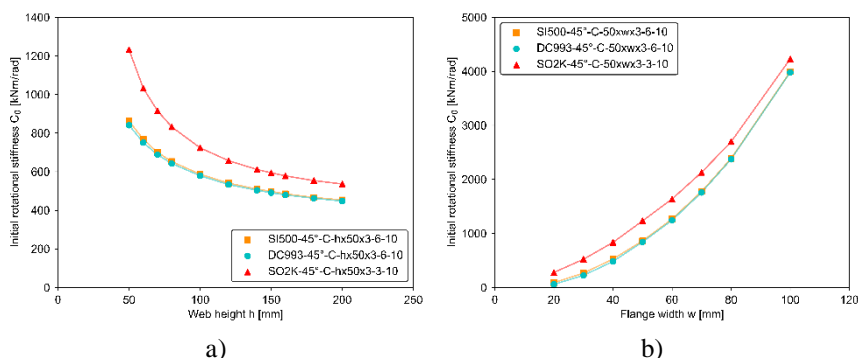


Fig. 19: Initial rotational stiffness C_0 [kNm/rad] as function of a) the web height h [mm] and b) the flange width w [mm] for all investigated adhesives.

Fig. 20 represents the initial rotational stiffness C_0 [kNm/rad] as a function of the section thickness t [mm] for configurations with 50x50xt, 100x50xt and 150x50xt steel sections for all investigated

adhesives. An increase in section thickness results in a significant increase in initial rotational stiffness due to an increased second moment of area combined with an increased weld area that successfully stiffens the corner configuration.

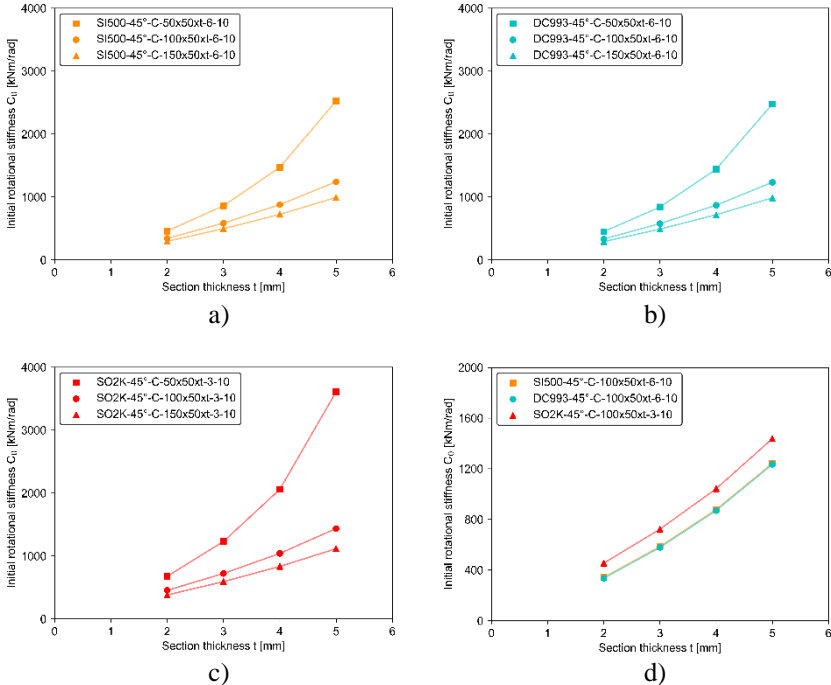


Fig. 20: Initial rotational stiffness C_0 [kNm/rad] for configurations with 50x50x3, 100x50x3 and 150x50x3 steel sections as function of the section thickness t [mm] for a) SI500, b) DS993, c) SO2K and d) a comparison between adhesives for configurations with 100x50x3 steel sections.

5. Conclusions

Current research on component level of bonded glass-steel frames subjected to in-plane loads focuses on small-scale specimen tests on single-lap or double-lap joints. However, as the geometry of the adhesive glass-steel joint changes near the corners of circumferentially bonded glass-steel frames, additional medium-scale tests on corner configurations gives additional insight in the local behaviour of the glass-steel joint. In this paper, the structural performance of welded steel corners, both not bonded and bonded with glass panes, are investigated to assess the in-plane load bearing capacity of these connections. The stiffness of both type of connections was experimentally investigated.

In a first experimental phase, tensile (T) and compressive (C) tests were conducted on steel corners welded in a 45°-configuration or 90°-configuration. The rotational stiffness of the corner was determined using the slope deflection method and the results were validated based on digital image correlation measurements. The initial rotational stiffness C_0 of the 90°-T-configuration differed

statistically significantly from the other configurations, i.e. the 45°-C-, 45°-T- and 90°-C-configuration. Therefore, in a second experimental phase, only a 45°-C-configuration and 90°-T-configuration were considered. These configurations were adhesively bonded with glass panes on both sides using SI500, DS993 and SO2K. The bonded specimens did not demonstrate a significant difference in values for the initial rotational stiffness when comparing the 45°-C-configuration with the 90°-T-configuration. The 45°-C-specimens bonded with SI500 had an initial rotational stiffness equal to 596.50 ± 22.24 kNm/rad, whilst for the specimens bonded with DS993 this value equalled 589.52 ± 28.84 kNm/rad. Specimens bonded with SO2K behaved significantly stiffer with a value of the initial rotational stiffness equal to 700.89 ± 10.05 kNm/rad.

A finite element model of the welded corner configurations without or with two-sided bonded glass panes, was validated and utilised to perform parametric studies. Based on the parametric study for the non-bonded specimens, figures were drawn that allow the determination of the initial rotational stiffness of the welded steel connection. These values can be implemented in analytical models for the calculation of steel structures with semi-rigid joints. For bonded specimens with SI500 and DS993, the glass thickness had a negligible effect on the initial rotational stiffness for adhesive joints with a thickness of 6 mm. In contrast, for SO2K with an adhesive thickness of 3 mm, the initial rotational stiffness increased with an increase in glass thickness. The influence of the glass thickness was important for low values of the adhesive thickness. The effect of the adhesive thickness on the value of the initial rotational stiffness was most important for values below 5 mm. An increase in flange width and thus in adhesive bite increased the value of the initial rotational stiffness, whilst an increase in the web height resulted in a decrease of the initial rotational stiffness. Eventually, increasing the section thickness beneficially affected the value of the initial rotational stiffness.

The results of medium-scale tests on corner configurations as obtained in this paper can be used for the implementation in mechanical models of (two-sided) bonded glass-steel units subjected to horizontal in-plane loads, i.e. bonded glass-steel façade elements that contribute to the building's stabilisation system. To validate the aforementioned statement, medium-scale and full-scale bonded glass-steel elements have to be experimentally tested for their horizontal in-plane load-bearing capacity. This will be subject of future publications with respect to research on two-sided bonded glass-steel façade units. When the

overall structural behaviour of such elements subjected to in-plane shear can be predicted based on small-scale and medium-scale tests, the number, hence also the cost, of full-scale tests can be significantly reduced. Based on this novel methodology, as suggested, a technical framework and design guidelines could be further elaborated allowing the introduction of novel bonded glass-steel façade elements into the market.

Acknowledgements

The authors would like to acknowledge the support of the company Polypane Glasindustrie NV in Temse, Belgium, for donating the glass panels and help with the production of the samples using DowSil™ 993. Soudal in Turnhout, Belgium, is thanked for the donation of the Soudaseal 2K adhesive. Permasteelisa group is acknowledged for the help with the production of the specimens with Sikasil® SG-500 at Scheldebouw nv in Middelburg, The Netherlands.

Conflict of interest

On behalf of all authors, the corresponding author states that there is no conflict of interest.

References

- [1] Belis J, Callewaert D, Van Hulle A. Bouwen met glas en adhesieven – praktische gids voor ontwerper en uitvoerder (in Dutch). Ghent University, 2011.
- [2] Luible, A. Stabilität von Tragelementen aus Glas (in German). Doctoral dissertation. Swiss Federal Institute of Technology Lausanne (EPFL), Switzerland, 2004.
- [3] Englhardt O. Flächentragwerke aus Glas - Tragverhalten und Stabilität (in German). Doctoral dissertation. University of Natural Resources and Life Sciences, Vienna, Austria, 2007.
- [4] Wellershoff F. Nutzung der Verglasung zur Aussteifung von Gebäudehüllen (in German). Doctoral dissertation. RWTH Aachen, Germany, 2006.
- [5] Mocibob D. Glass panel under shear loading – use of glass envelopes in building stabilization. Doctoral dissertation. Swiss Federal Institute of Technology Lausanne (EPFL), Switzerland, 2008.
- [6] Huveners EMP. Circumferentially adhesive bonded glass panes for bracing steel frames in facades. Doctoral dissertation.. Eindhoven University of Technology, The Netherlands, 2009.
- [7] Silvestru VA. Composite structural glazing systems – Towards transparent building envelopes with composite structural behaviour between glass panes and metal framing by adhesive bonding. Doctoral dissertation. Graz University of Technology, Austria, 2018.
- [8] Van Lancker B. Experimental and numerical investigation of two-sided bonded glass-steel façade units. Doctoral dissertation. Ghent University, Belgium, 2020.

- [9] Overend, M., Watson, J., Jin, Q. The selection and performance of adhesives for a steel–glass connection. *Int J Adhes Adhes*, 31(7), 2011, pp. 587-597.
- [10] Nhamoinesu, S., Overend, M., Silvestru, V. A., Englhardt, O. The mechanical performance of adhesively bonded steel-glass composite panels - Medium-scale tests and numerical models. In: Louter, C., Bos, F., Belis, J., Lebet, J.-P. (eds.) *Challenging Glass 4 & COST Action TU0905 Final Conference*, Lausanne, 2014, pp. 269-276.
- [11] Machalická, K., Horčíčková, I., Eliášová, M.. Shear adhesive connections for glass structures. *IOP Conference series: Mater Sci Eng*, 2015, 96:012069.
- [12] Machalická, K., Vokáč, M., Pokorný, P., Pavlíková, M. Effect of various artificial ageing procedures on adhesive joints for civil engineering applications. *Int J Adhes Adhes*, 97, 2020, article 102476.
- [13] Silvestru, V.A., Drass, M., Englhardt, O., Schneider, J. Performance of a structural acrylic adhesive for linear glass-metal connections under shear and tensile loading. *Int J Adhes Adhes*, 85, 2018, pp. 322-336.
- [14] Katsivalis, I., Thomsen, O., Feih, S., Achintha, M. Strength evaluation and failure prediction of bolted and adhesive glass/steel joints. *Glass Struct Eng*, 3(2), 2018, pp. 183-196.
- [15] Katsivalis, I., Thomsen, O. T., Feih, S., Achintha, M. Failure prediction and optimal selection of adhesives for glass/steel adhesive joints. *Eng Struct*, 201, 2019, article 109646.
- [16] Van Lancker B, Dispersyn J, Hertelé S, De Waele W, De Corte W, Belis J. Application of digital image correlation in linear structural adhesive glass-metal connection testing. In: *Proceedings of GlassCon Global Conference 2016*, Boston, 2016, p. 305-313.
- [17] Vandepitte D. *Berekening van constructies: bouwkunde en civiele techniek* (in Dutch). Story-Scientia, 1979.
- [18] Timoshenko SP. *History of strength of materials*. McGraw-Hill, 1953.
- [19] Haldimann M, Luible A, Overend M. Structural use of glass. *Structural Engineering Document (SED)*, International Association for Bridge and Structural Engineering, IABSE, 2008.
- [20] CEN. EN1993-1-3:2006: Eurocode 3 – Design of steel structures – Part 1-3: General rules – Supplementary rules for cold-formed members and sheeting. European Committee for Standardization, CEN, 2006.
- [21] Van Lancker B, De Corte W, Belis J. Calibration of hyperelastic material models for structural silicone and hybrid polymer adhesives for the application of bonded glass. *Constr Build Mater*, 2020, 254:article 119204.